Journal of Nuclear Materials 390–391 (2009) 398–403

Contents lists available at ScienceDirect

Journal of Nuclear Materials

journal homepage: www.elsevier.com/locate/jnucmat

3D analysis of impurity transport and radiation for ITER limiter start-up configurations

X. Zha [a,*], F. Sardei [a], Y. Feng [a], M. Kobayashi [b], A. Loarte [c], G. Federici [c]

[a] Max-Planck-Institut für Plasmaphysik, EURATOM Association, Boltzmannstrasse 2, Greifswald/Garching 85748, Germany
[b] National Institute for Fusion Science, Toki, Japan
[c] EFDA Close Support Unit Garching, Boltzmannstrasse 2, 85748 Garching, Germany

ARTICLE INFO

PACS:
52.40.Hf
52.55.Rk
52.65.Kj
52.65.Pp

ABSTRACT

Previous three-dimensional modelling of the ITER SOL plasma transport during the current ramp-up limiter phase with the EMC3-EIRENE code [M. Kobayashi et al., Nucl. Fus. 47 (2007) 61] has been extended to include the limiter-released Beryllium (*Be*) production, transport and radiation. The 3D density distributions of the single *Be* charge states and related line radiation have been simulated for two plasma densities and three plasma configurations during the ramp-up phase [G. Federici et al., J. Nucl. Mater. 363–365 (2007) 346]. The transport coefficients were also varied to check the sensitivity of the radiation to the transport. As expected, for all three configurations the radiated fraction of the SOL input power, P_{rad}/P_{SOL}, increases with the density at the last closed flux surface (LCFS). Preliminary results indicate largest P_{rad}/P_{SOL} for the 4.5 MA configuration, high density, high diffusivity case, $P_{rad}/P_{SOL} \approx 19\%$, *Be* concentration $\approx 16\%$ and $Z_{eff} \approx 2.5$ at the LCFS. These absolute numbers scale linearly with the assumed sputtering coefficients, but are rather insensitive to the initial energy of the sputtered *Be* atoms.

1. Introduction

A three-dimensional (3D) transport study of the ITER SOL [1] during the start-up limiter phase with the EMC3-EIRENE code [3,4] has shown that in the present design the two limiter modules introduce, in the presence of magnetic shear, a complex 3D topology, which significantly affects the power transport in the SOL and the power deposition onto the limiters.

In the first operational phase of ITER, Beryllium is planned to be the limiter-coating material primarily because (a) it is a low-*Z* material, which is fully ionised at thermonuclear plasma conditions, leading to low radiation losses, (b) it has good gettering properties for intrinsic oxygen. However, large physical sputtering rates of *Be* are expected for typical temperatures of order 100 eV in start-up limiter plasmas [5]. Resulting high impurity radiation could cool down the edge plasma in limiter configurations, triggering a radiation collapse of high plasma density discharges because of the low ohmic heating power [6]. This problem is more crucial for ITER than for smaller devices from the present generation of experiments such as JET, as for similar plasma densities and temperatures, plasma currents and impurity concentrations, the ohmic heating to the plasma scales inversely with plasma radius (a^{-1}), while impurity radiation losses from the plasma increase quadratically with plasma radius (a^2) [7,8].

2. The modelling code

Basic inputs to the EMC3-EIRENE code are the geometries of the boundary magnetic surfaces and of the plasma-facing components. The time evolution of the plasma magnetic surfaces during current ramp-up (Fig. 1(a)) is taken from equilibrium calculations for the reference ITER start-up scenario 2 (15 MA inductive current, 400 MW fusion power and $Q = 10$, Q being the ratio of fusion power to external heating power [8,9]). The computational domain includes the complete SOL from the LCFS up to the main chamber wall (Fig. 1(b)). The inner boundary ('upstream position') of the computational grid lies about 2 cm inside the LCFS at the limiter position, the grid is strongly refined near the limiter, where strong local gradients and grazing incidence of the field lines require a very high resolution.

EMC3-EIRENE solves a standard set of time-independent plasma fluid transport equations for mass, momentum and ions and electrons energy [10]. Drifts are not included. The cross-field diffusion coefficient $D_\perp$ is taken from measured density *e*-folding lengths scaled with respect to the plasma current for JET [11] and other divertor tokamaks, the cross-field conductivity $\chi_i = \chi_e$ is chosen such that the calculated ratios of density to temperature *e*-folding lengths equal those measured in JET and other divertor

* Corresponding author.
E-mail address: xuejun.zha@ipp.mpg.de (X. Zha).

0022-3115/$ - see front matter © 2009 Elsevier B.V. All rights reserved.
doi:10.1016/j.jnucmat.2009.01.310

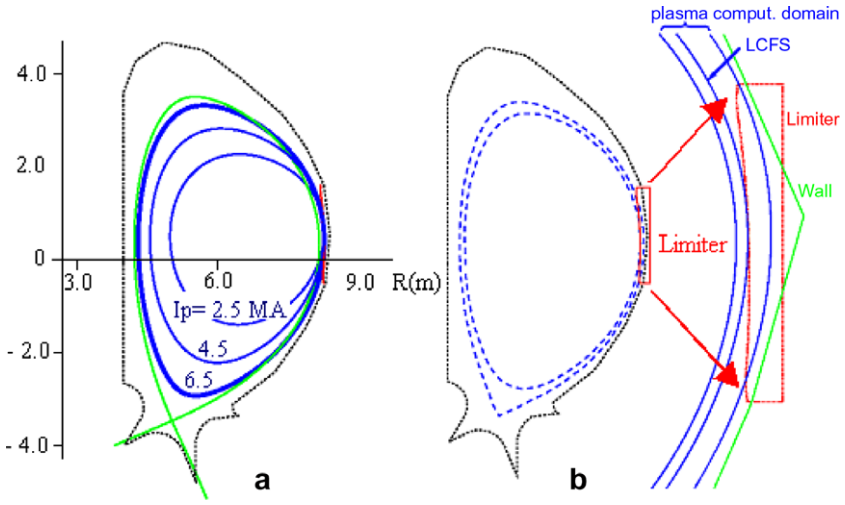

Fig. 1. (a) Time evolution of the limiter-defined plasma boundary during the current ramp-up phase, (b) poloidal cross-section of the computational domain covering the limiter SOL region.

tokamaks. Upstream boundary conditions are plasma density, zero momentum and heat power entering the SOL. Downstream boundary conditions at the limiter surface are the standard Bohm conditions [5].

For impurities (one species), the following mass and momentum transport model is implemented in the EMC3-EIRENE code for each ionisation stage Z [12]:

$$\nabla\cdot(n_Z V_{Z\|}b - D_Z b_\perp b_\perp\cdot\nabla n_Z) = S_{Z-1\to Z} - S_{Z\to Z+1} + R_{Z+1\to Z} - R_{Z\to Z-1}, \quad (1)$$

$$U_{Zi}(V_{Z\|} - V_{i\|}) = -b\cdot\nabla n_Z T_Z + n_Z Z e E_\| + n_Z Z^2 C_e b\cdot\nabla T_e + n_Z C_i b\cdot\nabla T_i, \quad (2)$$

with $T_Z = T_i$, $D_Z = D_\perp$, where the index Z labels impurity charge states, and the four terms on the rhs of Eq. (1) represent the ionisation (S) and recombination (R) processes. The term on the lhs of Eq. (2) models the friction with plasma ions, the last two terms on the rhs represent the thermal forces. The parallel E-field is determined by the parallel momentum equation for electrons:

$$N_e e E_\| + b\cdot\nabla n_e T_e + n_e C_e b\cdot\nabla T_e = 0. \quad (3)$$

The model applies to light impurities at small concentrations, $Z^2 n_z \ll n_e$, which means that the impurities affect the plasma only via radiation losses (trace-impurity model). The test-particle approach, which is valid for small radiation losses compared to the SOL input power, reduces the impurity transport study to a linear problem, allowing a linear scaling of the impurity densities and radiation losses with the sputtering yields without the need for iterative re-computation of the background plasmas. Upstream boundary condition for the impurities at the inner boundary surface of the computational domain is zero particle flux for each charge state. This condition is exactly satisfied by reflecting Monte Carlo particles at the boundary. In the EMC3 code, *Be* neutrals are started at the point of release from the limiter with a cosine distribution and constant energy. They are followed as Monte Carlo particles before and after ionisation.

3. Impurity sources

EMC3-EIRENE modelling shows that in the start-up limiter phase the plasma particle outflow is dominated by ions hitting the limiters. Therefore, only *Be* sputtering from ion bombardment and *Be* self-sputtering at the limiters are taken into account in this study. Effective *H–Be* sputtering yields including self-sputtering, Y_{eff}, and average energies of sputtered *Be* atoms, E_{sput}, are estimated from measured data [13,14] and from model calculations [15,16], respectively. Hereby, both Y_{H-Be} and Y_{Be-Be} are taken as functions of the incident energy at normal incidence and their enhancement due to deviation from normal incidence is taken into account, in the angle average and for rough surfaces, by taking twice the values at normal incidence [17]:

$$Y_{eff}(E_0) = 2Y_{\mathrm{H-Be}}(E_0)/(1 - 2Y_{Be-Be}(E_0)). \quad (4)$$

4. Parameter scan

As in the previous study mentioned in the introduction [1], we selected three limiter configurations defined by the plasma current I_p = 2.5, 4.5 and 6.5 MA (Fig. 1(a)). For each configuration two density cases were considered, 0.2 and 0.5 of the Greenwald limit [7], which cover the typical range of operation in large tokamaks such as JET. The SOL power, which results from Ohmic heating plus auxiliary heating minus radiation losses, was taken from start-up ITER simulations of the core transport with the ASTRA code [2]. The high density cases were also modelled with additional 50% of the respective SOL input power values to cover uncertainties of the core transport model in the estimation of the total power required to avoid radiative collapse at higher densities. The diffusion coefficients were scaled from JET limiter discharges with respect to the

Table 1
Scanned parameter range for three density cases, $\langle n\rangle = 0.2n_G$, $0.5n_G$ and $0.5n_G$ with +50% P_{SOL}, chosen from core transport simulation study for the ITER start-up configuration. n_G is the Greenwald density. The upstream density, n_{up}, was obtained as 20% of $\langle n\rangle$. $D_\perp$ is scaled from the JET limiter discharge with respect to the plasma current.

I_p (MA)	P_{SOL} (MW)	$D_\perp$ ($m^2\,s^{-1}$)	λ_T/λ_n	n_{up} ($10^{19}\,m^{-3}$)
$\langle 0.2 * n_G\rangle$				
2.5	1.0	1.0, 2.0, 3.0	1	0.12
4.5	2.0	0.3, 0.65, 1.0	1.5	0.17
6.5	3.0	0.2, 0.3, 0.4	1.5	0.22
$\langle 0.5 * n_G\rangle$				
2.5	1.3	1.0, 2.0, 3.0	1	0.30
4.5	2.6	0.3, 0.65, 1.0	1.5	0.44
6.5	4.0	0.2, 0.3, 0.4	1.5	0.54
$\langle 0.5 * n_G\rangle$ + 50% P_{SOL}				
2.5	2.0	1.0, 2.0, 3.0	1	0.30
4.5	4.0	0.3, 0.65, 1.0	1.5	0.44
6.5	6.0	0.2, 0.3, 0.4	1.5	0.54

plasma current and varied over a reasonable range as in [1]. The parameters of the scan are shown in Table 1.

According to the test-impurity model used, background plasmas were pre-calculated and fixed during the parameter scan over the 27 cases. In order to decouple the transport physics, which is considered essential in determining the scaling of the *Be* radiation, from the source effects, fixed values of the sputtering parameters, Y_{eff} = 1% and E_{sput} = 8 eV were used throughout the scan. In the next sections, actual values of the *Be* density, ionisation rate and radiation are obtained for the case with the largest P_{rad}/P_{SOL} *('worst case')* by linear upscaling the sputtering flux to the actual effective value of Y_{eff}.

The most relevant information of the scan, namely the total impurity radiation fraction of the SOL input power, is shown in Fig. 2. The analysis of this scan is facilitated by including the corresponding pictures of the total *Be* densities at the LCFS, $n_{Be,LCFS}$ (Fig. 3). For each configuration, the plasma recycling flux is found to increase with both the plasma upstream density and diffusion

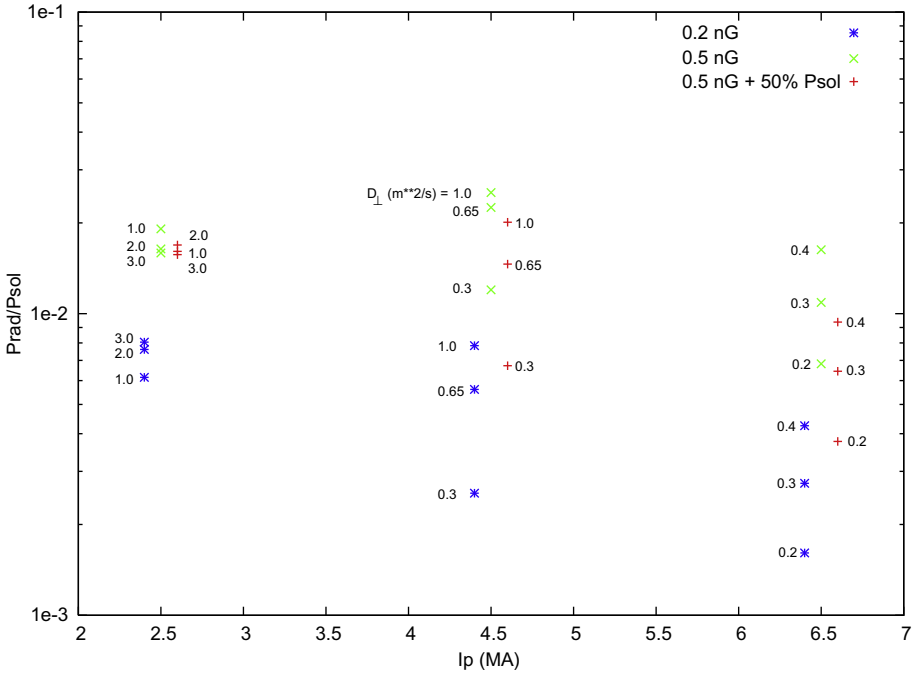

Fig. 2. *Be* impurity radiation fraction of SOL input power from a parameter scan covering, for three configurations, I_p = 2.5, 4.5 and 6.5 MA, three cases: $0.2n_G$, $0.5n_G$ and $0.5n_G$ with additional 50% P_{SOL}.

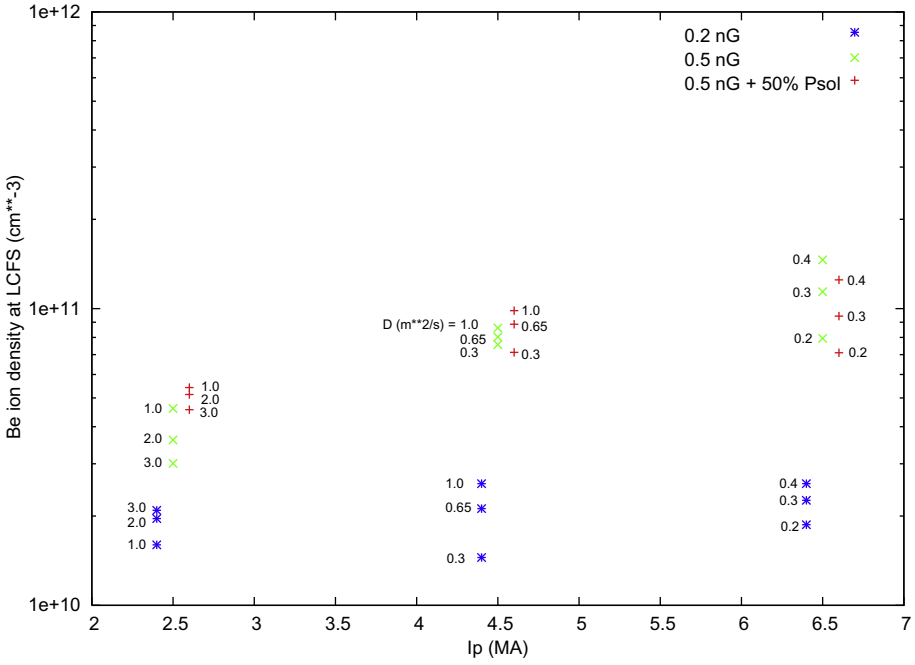

Fig. 3. *Be* ion densities at the LCFS for the analysed parameter scan.

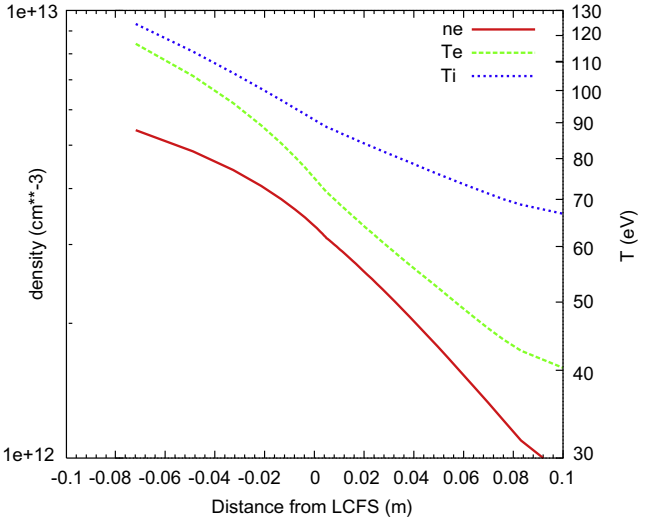

Fig. 4. Flux-surface averaged profiles of plasma density and temperatures for the reference case. The radial coordinate represents a flux-surface averaged radial distance. Its origin is the intersection of the LCFS with the outer midplane.

coefficient, scaling roughly as $\Phi_{recy} \propto {D_\perp}^{1/2}\, n_{up}$, as expected [5]. (Different P_{SOL} values for the single cases do not alter this trend.) In the test-particle approximation for impurities, the *Be* density is linearly coupled with the sputtering source and hence with the recycling flux. Therefore, a higher n_{up} raises Φ_{recy} and the impurity source, thereby increasing $n_{Be,LCFS}$, as shown in Fig. 3. However, $n_{Be,LCFS}$ results from the combined effects of source and transport. A larger $D_\perp$ for the background plasma raises the total recycling flux, thereby increasing $n_{Be,LCFS}$. On the other hand, a simultaneous co-increase in $D_\perp$ for *Be* will reduce $n_{Be,LCFS}$. Thus, a co-variation of $D_\perp$ for both the background plasma and the *Be* impurities leads to a trade-off between two competing processes, source and transport, in determining $n_{Be,LCFS}$. This makes an estimation of the $D_\perp$ -impact on $n_{Be,LCFS}$ very difficult. In fact, the 3D code did not show any simple scaling of $n_{Be,LCFS}$ with $D_\perp$ throughout the whole parameter range. Other effects such as the *Be* neutral source distribution and transport as well as the parallel *Be*-ion transport in the limiter SOL may become important for determining the $D_\perp$ -dependence of $n_{Be,LCFS}$. For example, the inverse scaling in the high density, high diffusivity case of the 2.5MA configuration shown in Fig. 3 could be explained by an increasing outward shift of the *Be* source distribution reflected by a factor-of-2 reduction of the core-ionisation fraction in the high n_{up}, high $D_\perp$ case. In the high density cases, 50% additional input power reduces the radiated fraction of the total input power during the current ramp-up (Fig. 2), but is not effective at early discharge conditions (2.5 MA).

5. Reference case

In the parameter scan, the largest P_{rad}/P_{SOL} was found for the 4.5 MA configuration, high density, high diffusivity case, as specified by the parameters $\langle n \rangle = 0.5\ n_G$, $P_{SOL} = 2.6$ MW, $D_\perp = 1.0\ \mathrm{m^2\ s^{-1}}$ (Table 1). This case has been analysed in more details and was taken as a reference case in this study.

In order to approach full ionisation at the inner computational boundary to eliminate boundary condition effects, the reference case was recalculated with a computational domain extended radially up to 8 cm inside the LCFS. The poloidally/toroidally averaged plasma density and temperature profiles for the reference case are shown in Fig. 4 over the flux-surface averaged radius. Their deviation from a simple exponential decay is due to both the complex L_c structure and the ionisation contributions within the SOL.

The average ion and electron temperatures over the limiter surface are $T_i \approx T_e \approx 45$ eV. These quantities belong to the limiter-shadowed short flux tubes and should be distinguished from the T_i, T_e in Fig. 4, which represent toroidally/poloidally averaged quantities over both the long and short flux tubes. T_e and T_i are typically flat over the relevant recycling zone of the limiter, which covers about 25% of the limiter surface. The flattening of T_e reflects the effect of the large decay lengths of the long flux tubes, which feed the short flux tubes by radial diffusion in the presence of shear (3D effect) [1,18,19]. T_i is reduced to the T_e level by additional ion

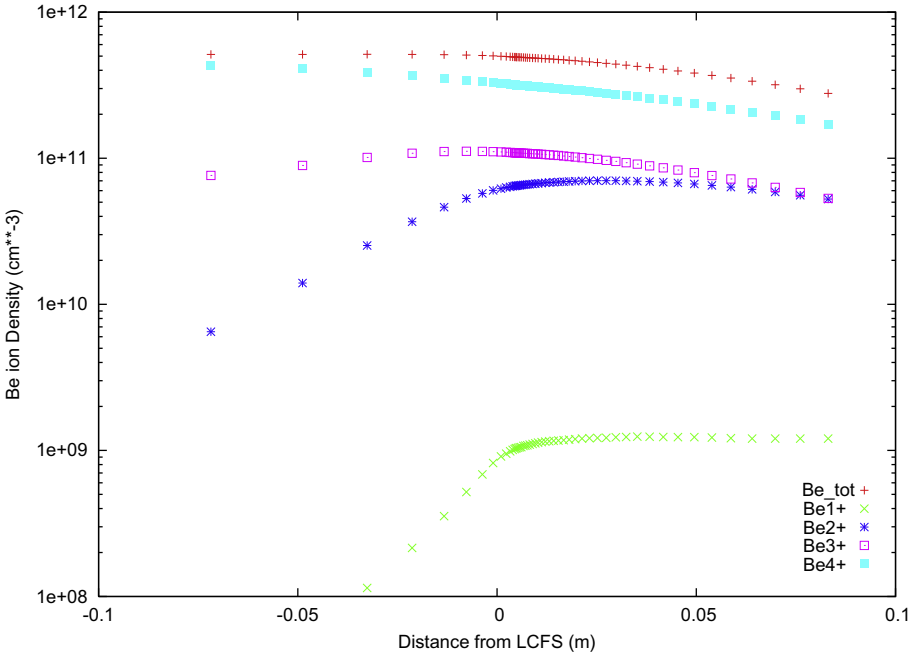

Fig. 5. *Be* charge-state density profiles for the reference case. The slopes of the profiles seen at the inner boundary reflect ionisation losses, not finite particle fluxes at the boundary. A zero particle flux condition for each charge state is exactly enforced by reflection of Monte Carlo particles.

energy losses in the limiter/core contact zone. These losses are related to a plasma density peak caused by particle stagnation in front of the limiter. The resulting cross-field particle diffusion carries plasma energy away from the limiter, which for ions is not replaced effectively by parallel transport. Moreover, high local recycling enhances the CX losses, which further decrease T_i. The averaged temperature at the limiter gives incident energies of $(E_0)_c = 220$ eV and $(E_0)_{Be-Be} = 630$ eV (for Be^{4+}). With these energy values an effective sputtering yield of 8% and an average sputtered energy of 8 eV are estimated from [13–16] and used in the code. The resulting profiles of the *Be* charge-state densities are shown in Fig. 5. The total radiation peaks at the LCFS (not shown here). The calculations show that the dominant contribution to the radiation comes from Be^{3+}. Although, the cooling rates of Be^{1+} and Be^{2+} exceed those of Be^{3+}, they are overcompensated by the higher density of Be^{3+}. This density is a factor of five below that of Be^{4+} at the upstream computational boundary, which is a good approximation for the expected full ionisation in the core.

For the reference (worst) case, the EMC3-EIRENE predicts a *Be* concentration of about 16% and $Z_{eff} \approx 2.5$ at the LCFS, and a 19% total *Be* radiation fraction of the SOL input power. This *Be* concentration marginally meets the validity of the adopted trace-impurity model (Section 2).

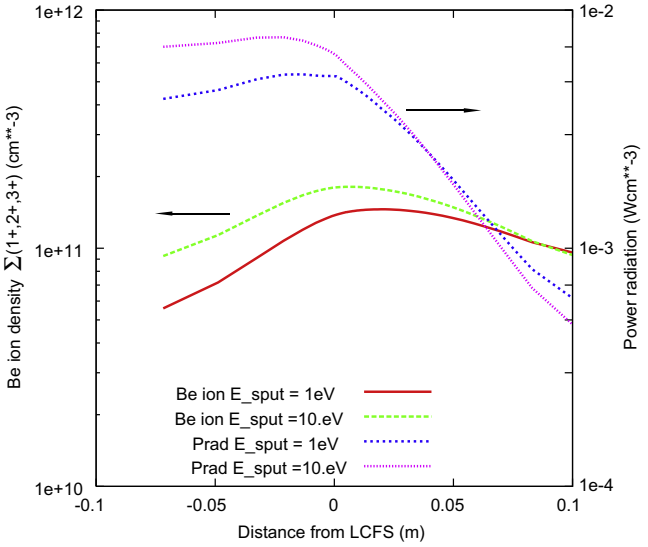

Fig. 7. Profiles of the *Be* ion densities and radiation power using $E_{sput} = 1$ and 10 eV.

6. Sensitivity studies

In order to assess the dependence of the results from uncertainties in the *Be* sputtering yield and the energy of the sputtered *Be* atoms, the sensitivity of the radiation to these parameters has been checked.

6.1. Sensitivity to the Be sputtering yield

From the used trace-impurity model, the *Be* radiation simply scales linearly with the effective sputtering yield. Because of this high sensitivity, the accuracy of the calculated radiation strongly depends on the accuracy of Y_{eff}. From experimental data and computational simulations, Y_{H-Be} and Y_{Be-Be} have flat maxima of ≈0.025 and ≈0.3 at 0.2 and 1 keV, respectively [13], which results, under the assumptions mentioned in Section 3, in a maximum of $Y_{eff} \approx 0.125$. These estimates have to be taken with caution, as in the energy range of interest to this study, Y_{H-Be} data from experiment have a spread of up to a factor of 2 [13]. For deuterium bombardment, the overall variation of Y_{eff} with energy is roughly twice as high, because of the higher collisional momentum transfer in the sputtering process.

6.2. Sensitivity to the sputtered energy

For the reference case, the sensitivity of P_{rad}/P_{SOL} to E_{sput} has been estimated by comparing two impurity transport simulations using the same background plasma and impurity source, but E_{sput} values differing by one order of magnitude in the relevant range

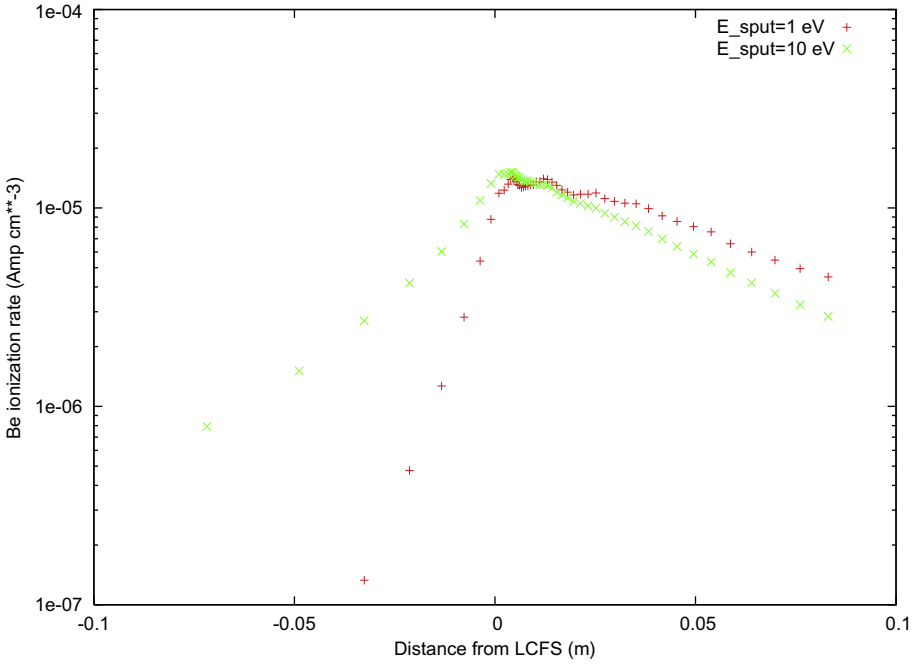

Fig. 6. Profiles of the *Be* ionisation rates using $E_{sput} = 1$ and 10 eV.

between E_{sput} = 1 and 10 eV. This includes all cases of the parameter scan and, in particular, the E_{sput} = 8 eV value used in the reference case. The resulting radial profiles of the *Be* ionisation rate, $n_{z0}n_eS_{z0}$, n_{Be} and P_{rad} for both simulations are shown in Figs. 6 and 7. Higher sputtered energies drive the released impurity atoms deeper towards the core, $d(n_{z0}\ v_{z0})/dx = -n_{z0}n_eS_{z0}$, with v_{z0} the velocity of the impurity atoms. Since for nearly constant n_eS_{z0} the decay length of the first-ionisation rate scales as $v_{z0} \propto (E_{sput})^{1/2}$, the two chosen energy values E_{sput} = 1 and 10 eV yield ionisation rate profiles with decay lengths into the core differing by roughly a factor of about 3 (Fig. 6). As a consequence of the deeper penetration of the impurity source, the densities of all *Be* charge states, and thus of n_{Be}, increase inside the LCFS (Fig. 7). This, in turn, leads to a rise of the total impurity radiation as the contributions from the SOL region are small compared to those from the core region close to the limiter. However, the resulting total radiation for the two cases (Fig. 7) differ only by about 30% in spite of the one-order-of-magnitude difference in E_{sput}, showing that the sputtered energy is not an essential parameter for the impurity radiation. (Energy values strongly deviating from this range are not relevant in the present analysis.)

7. Summary and conclusions

Three-dimensional investigation of the Be impurity transport and radiation has been started with the EMC3-EIRENE code for three ITER plasma start-up configurations and two plasma densities and for diffusion coefficients typical for operations of large tokamaks. In the first step, the *Be* impurities are treated as test particles in order to make a quick scan over the huge parameter space to identify critical parameter ranges for further detailed studies. Using the radiation fraction P_{rad}/P_{SOL} as a measuring quantity, the code has detected the high density and large diffusivity case in the 4.5 MA configuration as the 'worst' case with the largest radiation fraction of 19%. This result is obtained with an effective sputtering yield of 8% and an average sputtered energy of 8 eV, which are estimated (by taking both the H- and Be-projectiles into account) from the plasma temperatures at the limiter provided by the code. Both the parameters suffer from a large uncertainty of a factor about 2 due to angular dependence of the incident ions and surface topography. A sensitivity study has shown that the initial energy is not a sensitive parameter for the impurity radiation. However, P_{rad} linearly scales with the sputtering yield within the frame of the test-impurity model. A factor-of-2 larger sputtering yield would increase the already-remarkable radiation fraction up to a rather critical level. Thus, extended transport studies taking self-consistently the radiation into account are needed for more refined examinations of the critical situations.

Acknowledgements

X. Zha would like to express his deep gratitude for the essential support to this work received by EFDA CSU Garching, IPP Garching/Greifswald and JSPS-CAS Core-University Program on Plasma and Nuclear Fusion.

References

[1] M. Kobayashi et al., Nucl. Fus. 47 (2007) 61.
[2] G. Federici et al., J. Nucl. Mater. 363–365 (2007) 346.
[3] Y. Feng, F. Sardei, J. Kisslinger, J. Nucl. Mater. 266–269 (1999) 812.
[4] D. Reiter, Technical Report, Jül-1947, KFA Jülich, Germany, 1984.
[5] P.C. Stangeby, The plasma boundary of magnetic fusion devices, in: Plasma Physics Series, IOP Publishing Ltd, 2000.
[6] M. Greenwald et al., Plasma Phys. Control. Fus. 44 (2002) R27.
[7] A. Loarte, JET Limiter Ramp up/down studies, Seventh ITPA Divertor and SOL Physics Group, Donghua University, Shanghai, China, 2006.
[8] K. Behringer et al., in: Proceedings of 11th IAEA Conference Kyoto 1986, vol. 1, 1987, p. 197.
[9] Y. Gribov, Control System Design and Assessment (CSD), Appendix B: Magnetic Configuration and Poloidal Field Scenarios, N 19 RI 14 R0.1, August 2004.
[10] Y. Feng, F. Sardei, J. Kisslinger, et al., Contrib. Plasma Phys. 44 (2004) 57.
[11] S.K. Erents et al., Nucl. Fus. 28 (1988) 1209.
[12] Y. Feng, J. Kisslinger, F. Sardei, in: 27th EPS Conference on Controlled Fusion and Plasma Physics, Budapest, 2000.
[13] J. Roth, W. Eckstein, M. Guseva, Fus. Eng. Des. 37 (1997) 465.
[14] R. Behrisch, W. Eckstein (Eds.), Sputtering by particle bombardment, Topics in Applied Physics, vol. 110, Springer, Berlin/Heidelberg, 2007, pp. 1–20.
[15] W. Eckstein, Nucl. Instrum. and Meth. B 18 (1987) 344.
[16] W. Eckstein, Report IPP 9/132, 2002.
[17] J. Roth, private communication.
[18] Y. Feng, private communication.
[19] F. Sardei, Y. Feng, J. Kisslinger, et al., J. Nucl. Mater. 363–365 (2007) 511.